Editors' Suggestion

Multilayer graphenes as a platform for interaction-driven physics and topological superconductivity

Areg Ghazaryan ⬤,[1] Tobias Holder,[2] Erez Berg,[2] and Maksym Serbyn ⬤[1]

[1]*Institute of Science and Technology Austria, Am Campus 1, 3400 Klosterneuburg, Austria*
[2]*Department of Condensed Matter Physics, Weizmann Institute of Science, Rehovot 76100, Israel*

Motivated by the recent discoveries of superconductivity in bilayer and trilayer graphene, we theoretically investigate superconductivity and other interaction-driven phases in multilayer graphene stacks. To this end, we study the density of states of multilayer graphene with up to four layers at the single-particle band structure level in the presence of a transverse electric field. Among the considered structures, tetralayer graphene with rhombohedral (ABCA) stacking reaches the highest density of states. We study the phases that can arise in ABCA graphene by tuning the carrier density and transverse electric field. For a broad region of the tuning parameters, the presence of strong Coulomb repulsion leads to a spontaneous spin and valley symmetry breaking via Stoner transitions. Using a model that incorporates the spontaneous spin and valley polarization, we explore the Kohn-Luttinger mechanism for superconductivity driven by repulsive Coulomb interactions. We find that the strongest superconducting instability is in the p-wave channel, and occurs in proximity to the onset of Stoner transitions. Interestingly, we find a range of densities and transverse electric fields where superconductivity develops out of a strongly corrugated, singly connected Fermi surface in each valley, leading to a topologically nontrivial chiral $p + ip$ superconducting state with an even number of copropagating chiral Majorana edge modes. Our work establishes ABCA-stacked tetralayer graphene as a promising platform for observing strongly correlated physics and topological superconductivity.

I. INTRODUCTION

Graphene heterostructures in the presence of a superlattice potential induced by twist have opened new avenues to study interaction-driven physics [1–3]. In addition, superconductivity was discovered in a variety of twisted materials [2,4,5], whose mechanism remains debated. In a parallel development, studies of rhombohedral trilayer graphene *without* a moiré superlattice recently revealed interaction-driven ferromagnetic transitions [6] and superconductivity [7]. Superconductivity has also been identified in Bernal-stacked bilayer graphene [8,9]. The superconducting state is unconventional, at least in the sense that it far exceeds the Pauli limit for an in-plane magnetic field. These discoveries call for a detailed study of multilayer graphenes from the viewpoint of realizing interaction-driven symmetry broken phases, including superconductivity, which is addressed in the present paper.

Conventional graphite is composed of graphene layers arranged in the so-called Bernal stacking, ABAB..., where A and B denote two inequivalent graphene monolayers that are stacked in transverse directions. The study of interaction-driven physics in the bilayer AB graphene—one of the most-studied two-dimensional materials—has a long history [10–15]. Its immediate relatives, trilayer ABA [16–20] and tetralayer ABAB [21–24] graphenes, have received considerably less attention to date. Moreover, the observation of interaction-driven phenomena in trilayer and tetralayer Bernal stacks remains mostly limited to the regime of strong magnetic fields [19] or suspended samples [21,25].

In contrast to Bernal stacking, the so-called rhombohedral stacking is less stable, and thus less common. The simplest rhombohedral representative is ABC graphene, which displays much richer interaction physics [6,26] and even superconductivity when subjected to a perpendicular electric field [7]. Beyond three layers, transport [27] and scanning tunneling microscopy [28] studies in ABCA graphene revealed the development of a large gap at the neutrality point. Finally, thicker rhombohedral stacks were considered [29,30], also revealing important interaction effects near charge neutrality.

The dominant role of interaction effects in rhombohedral graphene, as compared to its Bernal allotrope, is naturally explained by a much higher density of states (DOS) in the rhombohedral case. In particular, if one ignores further-neighbor hopping in the tight-binding model, the rhombohedral stacks of n layers have an energy dispersion that depends on crystal momentum k away from the corner of the Brillouin zone as $\pm |k|^n$, leading to a diverging DOS at charge neutrality for $n > 2$ [31]. A transverse electric field that breaks inversion symmetry gaps out the band touching, leading to an even flatter dispersion that scales as k^{2n} near the bottom of the conduction band and top of the valence band. A gap may also open by interactions at the neutrality point [32,33]. However, already for ABC trilayer graphene, the aforementioned approximation ignores particle-hole asymmetry, trigonal warping, and other details of the band structure that are known to be important from experiments and from density functional theory calculations [33,34].

This highlights the need for a theory of interaction effects in multilayer graphene which incorporates the realistic

band structure, extending the theory developed for bilayer and ABC trilayer graphene [35–44]. The rich physics of bilayer and ABC graphene away from the neutrality point suggests multilayer graphene stacks as promising candidates for the realization of symmetry-broken phases and superconductivity.

In this paper, we seek to identify the most promising multilayer graphene stacks for realizing correlated physics and exotic superconductivity. To this end, we systematically study the noninteracting DOS of different multilayer structures. We identify the ABCA stacks of tetralayer graphene as the most promising candidate with the highest available DOS, which is further enhanced by the transverse electric field. For a larger number of layers, we argue that stronger screening of the electric field precludes any further enhancement of the noninteracting DOS. Therefore, in the remainder of our paper, we focus our attention on ABCA graphene.

ABCA graphene exhibits a rich fermiology as a function of density and transverse electric field with a variety of distinct Fermi surface (FS) types. This complex fermiology is due to the trigonal warping and particle-hole asymmetry which we include in our band structure model. We then consider the effect of interactions. Using a Stoner model, we identify regions of density and transverse electric fields that favor spin and valley symmetry-broken phases. Finally, we study the leading superconducting instabilities within the Kohn-Luttinger scenario of superconductivity [45–50]. Within this approach, we identify the most promising regions of the phase diagram where the critical temperature of the superconducting instability may be accessible experimentally. Importantly, for a certain range of parameters, a superconducting instability with p-wave pairing appears for a singly connected FS in each valley, thereby realizing a topological superconducting phase in ABCA tetralayer graphene. The topological superconductivity theoretically predicted in our paper does not require strong doping [51–53], and could be experimentally verified using transport and tunneling measurements.

We note that superconductivity in the surface states of bulk rhombohedral graphite was considered in Refs. [54,55]. These works assumed the presence of attractive interactions and demonstrated the enhancement of the critical temperature due to the flat-band character of the surface states in bulk graphite. In contrast, here we consider quasi-two-dimensional systems with only few layers, which allows the application of a transverse electric field so the carrier density can be changed by gating. Thus, we do not operate near the neutrality point, instead considering a finite carrier density and strong inversion-breaking electric fields. Moreover, we rely on the strong Coulomb repulsion that first gives rise to symmetry-broken phases via Stoner transitions, and at the same time acts as a pairing glue within the Kohn-Luttinger mechanism. In a different direction, superconductivity was analyzed for various graphene stackings using renormalization group [52,56].

II. SURVEY OF MULTILAYER GRAPHENE BAND STRUCTURES AND DENSITY OF STATES

We begin with a survey of band structures and DOS of graphene multilayers with different stackings. We consider systems up to four layers. Adding more layers does not introduce qualitative changes compared to tetralayers and may

prevent control of layer potentials by gating in experiments due to the enhanced screening (see Appendix A). The considered multilayers include Bernal stacked bilayer (AB), trilayer (ABA), tetralayer (ABAB), and corresponding rhombohedral stacked allotropes (ABC, ABCA), see Fig. 1(a). In addition, in the Appendix A, we consider the mixed stacking configuration ABCB, which was recently realized experimentally [57]. The corresponding Hamiltonians are written in the basis $(A_1, B_1, A_2, B_2 \dots)$, and the size of the Bloch Hamiltonian matrix is thus $2n \times 2n$, where n is the number of layers; see Appendix A. Stackings AB, ABC, ABAB, and ABCA feature an inversion center, while ABA graphene has a mirror symmetry. We also consider the presence of a layer asymmetry potential due to the perpendicular electric field, Δ_1 (defined such that the energy difference between the outer layers is $2\Delta_1$, and the energy varies linearly with the layer index). Examples of the low-energy band structures along the k_x direction are shown in Fig. 1(a) for a relatively strong but experimentally feasible value of $\Delta_1 = 60$ meV. Only the AB, ABC, and ABCA stackings possess a gap proportional to the applied electric field at charge neutrality. Including the trigonal warping and particle-hole asymmetry leads to a rich low-energy dispersion, with multiple FS topologies separated by Van Hove singularities (VHSs). As an overall trend, the DOS increases with increasing layer number. It should be noted that the wave functions of the low-energy bands of rhombohedral graphene stacks are mostly localized on the outer layers, intuitively corresponding to (hybridized) edge states [58]. In the three-dimensional limit, rhombohedral graphite is gapless, possessing Dirac nodal lines [59–62]. Thus, we expect stronger screening and the appearance of multiple low-energy bands for thicker rhombohedral stacks.

Figures 1(b) and 1(c) show the dependence of the DOS on charge density for different stackings for $\Delta_1 = 0$ meV and $\Delta_1 = 60$ meV, respectively. The top plots in Figs. 1(b) and 1(c) show the DOS of Bernal stacks, revealing that AB bilayer graphene has the highest DOS at large displacement fields in the Bernal family. The bottom plots in Figs. 1(b)–1(c) compare the AB stacking with the trilayer and tetralayer rhombohedral stacks, illustrating the greatly increased DOS of the latter. Notably, ABCA stacking features the largest DOS for a broad region in density, making it a promising candidate for interaction-driven physics. We will now explore its properties in detail.

III. BAND STRUCTURE OF ABCA GRAPHENE

To reveal the large number of FS topologies and the rich structure of the DOS of ABCA, we plot DOS as a function of charge density n_e and layer asymmetry Δ_1 in Fig. 2(a). Δ_1 is proportional to the applied electric field, but the precise form of the relation is determined by the screening in the system. In the Appendix A, we consider Hartree-type screening and show that values of $\Delta_1 = 120$ meV can be realized in experiments through the application of a displacement field strength of $\sim$2 V/nm.

On the hole side, $n_e < 0$, we observe in total five different FS topologies (ignoring for simplicity the region with $\Delta_1 \lesssim 2$ meV, where FS topology is complex and not relevant for the current discussion). In particular, a VHS divides regions with
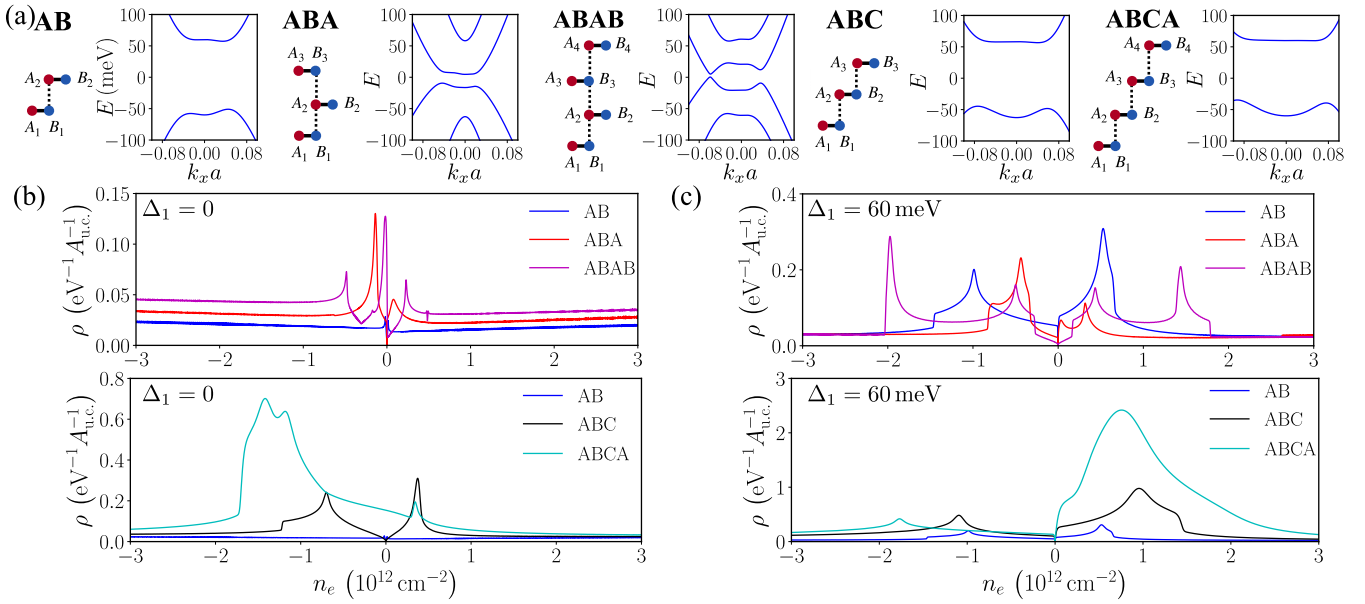
FIG. 1. (a) Stacking order and corresponding energy dispersions for multilayers. The displacement field is $\Delta_1 = 60$ meV. The DOS as a function of the charge density is shown for $\Delta_1 = 0$ meV (b) and $\Delta_1 = 60$ meV (c). Comparing the top plots in panels (b) and (c) reveals that among Bernal stacks, AB graphene has broad regions with an enhanced DOS for large Δ_1. Bottom plots in (b) and (c) show that the DOS of ABC and ABCA graphene surpasses AB graphene by almost an order of magnitude.
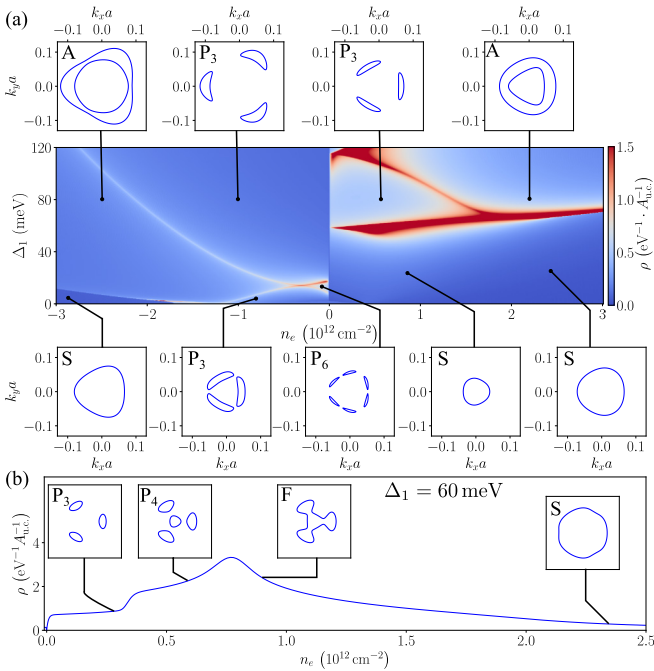

FIG. 2. (a) Color plot of the DOS ρ for ABCA multilayer as a function of displacement field Δ_1 and carrier density n_e. Different representative Fermi surface geometries are shown that are separated by VHSs. Letters next to the Fermi surfaces designate different topologies, including single Fermi surface (S), three pockets (P_3), four pockets that include a central FS (P_4), six pockets (P_6), and annular geometry consisting of two concentric Fermi surfaces (A). (b) Cut of the density of states for $n_e > 0$ at fixed value of $\Delta_1 = 60$ meV that reveals the existence of a single FS that is severely corrugated, taking a flower shape (F).

FSs of three pockets denoted as P_3, annular (A), and a simple single FS (S) in each valley. Note that for higher density range $n_e > -1 \times 10^{12}$ cm^{-2}, increasing Δ_1 only changes the direction of the three pockets, corresponding to π rotation of the pockets around $\mathbf{k} = 0$ point [see top and bottom P_3 panels on the hole side of Fig. 2(a)]. This transition is accomplished by having a six-pocket FS (P_6) in the vicinity of the VHS. Overall, the FS topology of ABCA on the hole side is similar to ABC trilayer graphene [6] with a somewhat enhanced DOS. This similarity suggests that the Stoner ferromagnetism and superconductivity mediated by electron-electron interactions will be qualitatively similar in both systems [6,36].

The electron side ($n_e > 0$) of the phase diagram of ABCA is richer and qualitatively differs from the case of the ABC graphene. For small values of Δ_1, there is only a single trig-onally warped FS (S). Notably, the direction of the trigonal distortion (warping) is reversed upon increasing the charge density. This reversal is illustrated by the two insets at the bottom right corner of Fig. 2(a), that both show a simple FS that increases in size and changes the distortion orientation. In the Appendix A, we present the effective 2×2 model of the Hamiltonian of ABCA graphene stacks that explains the flipping of the trigonal warping. At the density where this flipping occurs, the FS possesses sixfold symmetry.

For larger values of Δ_1 exceeding 80 meV, the FS tran-sitions from the three-pocket regime (P_3) to an annulus (A). This transition is similar to the one observed in the ABC trilayer [6] but is associated with considerably higher values of the DOS. In the range of $\Delta_1 = 60-80$ meV, the diagram shows a higher order VHS. In the Appendix B, we zoom into that region and show that the high DOS there can be attributed to the existence of several higher order VHSs located nearby in the parameter space. To highlight the complexity of FS

topologies, we show the density dependence of the DOS at a fixed value $\Delta_1 = 60$ meV in Fig. 2(b). For this Δ_1, we observe a transition between P_3 and P_4 FSs, see inset of Fig. 2(b). Moreover, we observe the merging of four pockets into a severely corrugated flower-shaped singly connected FS (F). Although such topology of the FS is continuously connected to the single contour FS (labeled as S) at larger densities, it will play an important role in the subsequent discussion, as it allows for the realization of topological superconductivity.

IV. STONER AND SUPERCONDUCTING INSTABILITIES IN ABCA GRAPHENE

After considering the noninteracting DOS of ABCA graphene, we address interaction effects. Inspired by the experimental results for ABC trilayer graphene [6], we first address the emergence of Stoner ferromagnetism. After understanding the sequence of Stoner transitions, we investigate the leading superconducting instability.

A. Stoner phase diagram

We consider effects of the electron-electron interaction and the possibility of symmetry-broken phases by means of a simple rigid band Stoner model which has been applied to twisted bilayer and ABC trilayer systems [6,63]. The noninteracting bands are fourfold degenerate due to the spin and valley (denoted collectively as isospin) symmetry. Interaction effects can lead to spontaneous symmetry breaking, lowering the original fourfold flavor degeneracy. Assuming an SU(4)-symmetric form of the interaction, one naturally obtains phases with threefold degenerate, twofold degenerate, and nondegenerate bands. Experiments in ABC trilayer graphene [6] did not reveal any regions with threefold degenerate bands, a finding that can be attributed to the existence of lattice-scale interactions that break the SU(4) symmetry of the Coulomb interaction. We account for such terms phenomenologically by adding a Hund's-type contribution to the interactions that couple the spins of electrons from the two valleys.

The rigid Stoner model is defined via the grand potential per area,

$$\frac{\Phi}{A} = \sum_\alpha E_0(n_\alpha) + V_{\text{int}} - \mu \sum_\alpha n_\alpha, \qquad (1)$$

where $E_0(n_\alpha)$ is the kinetic energy calculated from the noninteracting band structure for flavor α with the charge density n_α and μ is the chemical potential. The interaction potential V_{int} is taken as

$$V_{\text{int}} = \frac{UA_{\text{u.c.}}}{2} \sum_{\alpha \neq \beta} n_\alpha n_\beta + JA_{\text{u.c.}}(n_1 - n_3)(n_2 - n_4). \qquad (2)$$

Here $1 = \{K, \uparrow\}$, $2 = \{K', \uparrow\}$, $3 = \{K, \downarrow\}$, $4 = \{K', \downarrow\}$, and $A_{\text{u.c.}} = \sqrt{3}a^2/2$ is the area of unit cell, U is the valley and spin-isotropic interaction constant, and J is the intervalley spin-exchange Hund's rule coupling constant, which explicitly breaks SU(4) symmetry. $J < 0$ ($J > 0$) favors a valley-unpolarized ferromagnetic (antiferromagnetic) phase when only two flavors are occupied. To determine the realized phase for each chemical potential,, we minimize the grand potential for interaction strengths $U = 15$ eV and $J = -4.5$ eV.
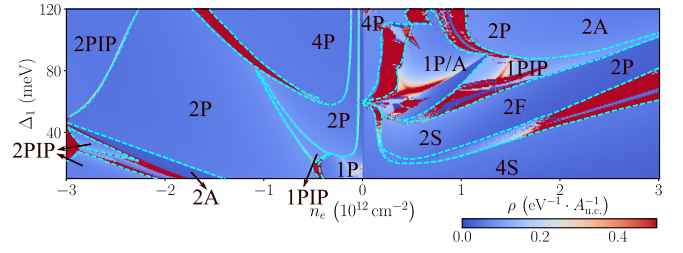

FIG. 3. Stoner phase diagram for interaction strengths $U = 15$ eV and $J = -4.5$ eV. Numbers denote the degeneracy of the phase and letters denote the topology of Fermi surfaces according to Fig. 2. For example, 2A is a region where a twofold degenerate annular Fermi surface is realized. For the case of multiple pockets, we use the label P without differentiating between different numbers of pockets (P_3, P_4, etc.). PIP denotes regions with partial isospin polarization. In the PIP regions, we do not distinguish FS topologies. Different phases are separated by cyan dashed lines.

The model thus includes two parameters for the interactions: U, which controls the strength of the SU(4) symmetric part of the Coulomb repulsion, and the Hund's coupling J, which sets the magnitude of terms breaking SU(4) symmetry. Using this parametrization, it is possible to qualitatively capture the phase diagram of ABC trilayer graphene [6], using values of $U = 30$ eV and $J = -9$ eV. Expecting that interaction strength is weaker in ABCA tetralayer graphene, since adding more layers brings additional energy bands closer to the neutrality point and enhances screening, we use $U = 15$ eV and $J = -4.5$ eV. Our choice of $J < 0$ implies that the system prefers ferromagnetic ordering. This means that a doubly degenerate phase will be spin polarized and valley unpolarized as was observed in the ABC trilayer [6].

Figure 3 reveals the complex phase diagram obtained from the rigid Stoner model. Due to the considerable magnitude of the Hund's ferromagnetic term, we do not observe phases with threefold degeneracy. At low values of Δ_1, we do not observe any symmetry-broken phases in the electron-doped side, whereas on the hole-doped side ($n_e < 0$) we see the sequence 4P, 2PIP, 2A, 2P, 1P of symmetry-broken phases, where the numbers denote the degeneracy of the phase, while letters denote the FS topology (the notation follows Fig. 2, except for the case of multiple pockets, in which case we do not differentiate between different numbers of pockets and use the general label P). PIP corresponds to the partially isospin polarized phase, where, for example, for 2PIP all four flavors are filled, but two have smaller filling compared to the remaining two. For PIP phases, we do not differentiate between phases with distinct FS topologies. Upon increasing the perpendicular electric field, extended regions of twofold degenerate phases develop on the electron side with multiple pockets, simple or an annular FS. Moreover, in the parts of the 2S region for positive densities ($n_e \approx 1.5 \times 10^{12}$ cm^{-2}), the flower-type geometry of the FS is realized. This will have important consequences on superconducting instabilities for the charge densities and asymmetry potential values where these phases are realized. At even higher values of Δ_1, the 2A region prevails, while at lower densities one also observes a region of single-degenerate FS (1P/A).

Finally, let us comment on the choice of the interaction parameters U and J and their effect on the phase diagram. In the Appendix C, we present results for the phase diagram with parameters identical to the ABC interaction strength used in Ref. [6]. In that latter scenario, the significantly larger interaction strength suppresses the PIP phases in the phase diagram. In addition, since the spontaneous symmetry breaking is most prominent close to band edges and lower densities, the increased interaction strength results in stronger symmetry breaking in the regime of small densities. Generically, the increased prevalence of symmetry-broken phases suppresses superconductivity, since the growth of the DOS in the normal state (conducive to superconductivity) is preempted by a Stoner instability.

B. Leading superconducting instabilities

We consider the potential superconducting instabilities of ABCA graphene using the band structure as obtained from the Stoner instability analysis. To this end, it is henceforth assumed that pairing emerges due to electron-electron interactions by the Kohn-Luttinger mechanism [45–47,49]. In this mechanism, attractive interaction between electrons is mediated through electron-hole fluctuations of electronic fluid. We account for these fluctuations through the random phase approximation (RPA), as in Ref. [36].

To obtain the pairing interaction, we consider screened Coulomb interaction between the electrons $V_{0,\mathbf{q}} = \frac{2\pi e^2}{\epsilon q}\tanh(qd)$, where ϵ is the dielectric constant of ABCA graphene and d is the distance to the metallic gates located on both sides of the sample. We use $\epsilon = 4$ and $d = 36.9$ nm. To incorporate electron-hole fluctuations, we use RPA,

$$V_{\mathbf{q}} = \frac{V_{0,\mathbf{q}}}{1 + \Pi_{0,\mathbf{q}}V_{0,\mathbf{q}}}. \tag{3}$$

This polarization function is proportional to N, $\Pi_{0,\mathbf{q}} \propto N$, where N is the number of occupied flavors and this controls both the screening and strength of superconducting instability (see Appendix D). Coupling constant λ is obtained from diagonalizing the eigenvalue equation $\mathcal{M}(V_{\mathbf{q}})\Delta_{\mathbf{k}} = \lambda\Delta_{\mathbf{k}}$, where $\mathcal{M}(V_{\mathbf{q}})$ is a linear operator, which is proportional to vertex of scattering of a pair of electrons from one momentum to the other on a FS. The largest eigenvalue λ corresponds to the leading superconducting instability, and the shape of the wave function may be used to infer the corresponding symmetry of the order parameter. For the case of p-wave symmetry, the nature of the order parameter below T_c can be inferred from the Ginzburg-Landau energy functional. Quite generally, when system possesses C_3 symmetry, a chiral superconducting state is preferred [36].

Let us comment on the treatment of spin and valley degrees of freedom that affect the pairing symmetry [64]. Due to $\text{SU}(2) \times \text{SU}(2)$ symmetry of the Hamiltonian spin-singlet (valley-triplet) and spin-triplet (valley-singlet) pairings are degenerate in our treatment. To lift that degeneracy, we need to consider short-range intervalley Hund's coupling. Following the general treatment from our previous work [36], which relies on an experimental finding that ferromagnetism is the dominant instability in the system in s-wave (p-wave) channels, spin-triplet (spin-singlet) pairing will be preferred.

Obviously, this argument applies in the regime when the degeneracy is not lifted due to the Stoner mechanism. In the regime where Stoner mechanism has lifted spin degeneracy and the normal phase is spin polarized, only spin-triplet pairing is possible.

We use the FSs and structure of noninteracting wave functions obtained earlier for the FSs with broken degeneracy due to Stoner mechanism. The parameter $N = 4$ (no broken symmetry) or 2 (twofold degenerate bands) controls the number of occupied flavors, thereby affecting the screening. We assume that phases with $N = 1$ are valley polarized, and thus have no superconducting instability. As noted in Sec. III, on the hole side the noninteracting phase diagram is qualitatively similar to the hole side in ABC trilayer graphene. Therefore, here we concentrate on the electron side of the phase diagram and on the new superconducting phases that were not present in ABC trilayers.

After obtaining the effective electron-electron interaction within RPA, $V_{\mathbf{q}}$, we compute the superconducting coupling constant λ from the linearized BCS gap equation. In the weak coupling approximation, λ determines the superconducting critical temperature according to $T_c = We^{-1/\lambda}$ with W being an energy cutoff, typically of the order of the Fermi energy. Alongside λ, we also study the gap function to infer the symmetry of the order parameter of the superconducting phase.

First, we investigate the behavior of the coupling constant at a relatively high value of Δ_1. In that case, the FS geometry changes from P_3 to annular. The presence of two FS contours results in considerable enhancement of superconductivity due to the Kohn-Luttinger mechanism [48,50,65]. Similar to the ABC trilayer case, we find the dominant instability to have p-wave symmetry, both for $N = 4$ and $N = 2$ (see Fig. 4). For a C_3 symmetric system, the quartic term in the free energy then favors a chiral $p + ip$ state below T_c [36]. In addition, we also find a small region with extended s-wave pairing (not shown).

Next, we combine the superconducting ordering tendencies with the Stoner phase diagram to identify regions where flavor degeneracy due to symmetry breaking is compatible with the normal phase of superconductor. As is clear from Fig. 4, for twofold degeneracy ($N = 2$) there are indeed regions of large λ which are not affected by the Stoner instability. Notably, assuming that the $N = 2$ state is spin polarized, we predict the realization of spin-triplet superconductivity with $p + ip$ symmetry of the order parameter. However, despite the presence of p-wave pairing, the superconducting phase is not topological. The reason for this is the two contours of the annular FS, which have opposite Chern numbers and overall add up to a vanishing Chern number. When comparing the results of the ABCA tetralayer with the ABC trilayer, the coupling constant λ for ABCA graphene is considerably larger. As mentioned earlier, this is related to the enhanced DOS of ABCA. Therefore, we expect the superconducting instability to be more robust than for the ABC trilayer.

C. Regime of topological superconductivity

For somewhat lower values of Δ_1, when a single, simply connected FS is present (see S and F contours in Fig. 2), topological superconductivity can be realized. To this end,
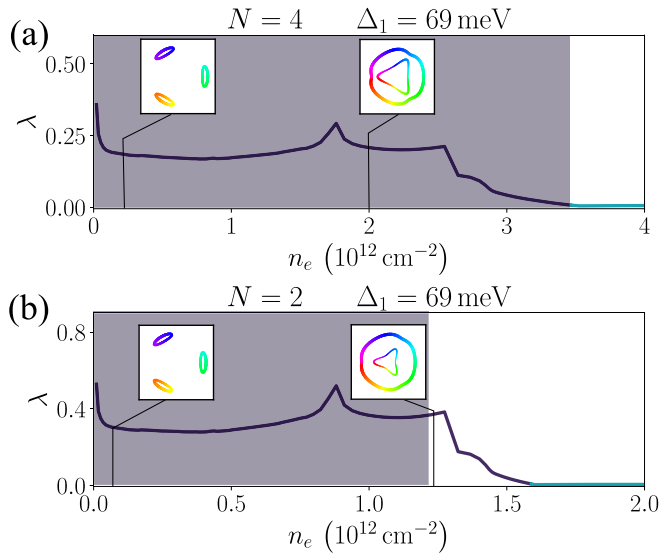
FIG. 4. Dimensionless superconducting coupling constant λ in ABCA tetralayer graphene as a function of density for $\Delta_1 = 69$ meV, assuming a degeneracy $N = 4$ for (a) and $N = 2$ for (b). In both cases, there is a very weak instability toward pairing in a high angular momentum channel at high densities (cyan color), followed by a much stronger p-wave pairing instability at lower densities (violet color). Shaded regions correspond to the range of densities that are inaccessible at the given degeneracy due to occurrence of the Stoner phase transition which decreases the degeneracy and changes the Fermi surface. Insets show Fermi surfaces and color denotes the phase of the order parameter, visually representing the chiral nature of the state.

FIG. 5. Focusing on the superconducting instability in the regime of twofold degenerate Fermi surfaces ($N = 2$) reveals a range of densities with intermediate values of $\lambda \geqslant 0.05$ and a single, simply connected Fermi surface. This situation is realized for $\Delta_1 = 42$ meV (a) and $\Delta_1 = 60$ meV (b) and leads to topological superconductivity.

we focus on the case when the Stoner transition reduces the FS degeneracy to $N = 2$ and study the density dependence of λ for two different values of Δ_1. Figure 5(a) corresponds to the value of $\Delta_1 < 45$ meV, when the FS contour is trigonally distorted and switches the direction of the trigonal distortion as a function of electron density. At the position where the direction of trigonal distortion is changed, the FS enjoys an approximate sixfold rotation symmetry, resembling a distorted hexagon. This shape of FS shows features of nesting, leading to enhancement of static polarization at nonzero momenta and also enhancing superconducting instability. The peak of DOS appears at smaller densities than the position where trigonal warping direction is flipped (not shown). Since the DOS also affects superconducting instability, the coupling constant and, correspondingly, the critical temperature shows a maximum at the density which is in between the densities of peak of DOS and hexagonal FS. The maximal values of λ in this regime are lower than those obtained for the annular FS (cf. Fig. 4). Nevertheless, the enhancement of λ suggests that enhancement of the symmetry of the FS due to a change in the trigonal warping direction gives rise to sizable critical temperatures within the framework of the Kohn-Luttinger approach, even in the absence of a multipocket FS.

The superconducting state illustrated in Fig. 5(a) is topologically nontrivial. For intermediate values of the charge density, the pairing is p wave, and we expect the resulting order parameter to have $p + ip$ character. For $N = 2$, there is a
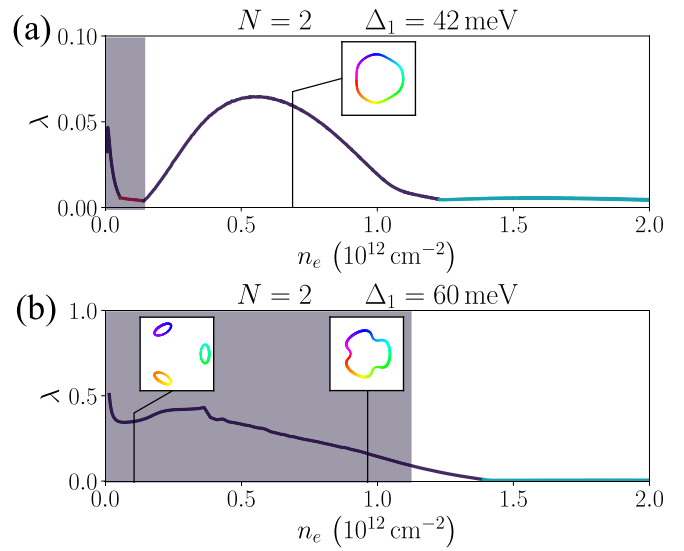
single FS in each valley. Each FS has a Chern number of one, so in total the system has a Chern number of two. Notably, for this value of Δ_1, the Stoner instability that further reduces the valley degeneracy occurs at lower electron densities. Thus, we predict a dome-shaped superconducting region as a function of carrier density, terminated by Stoner transition at low densities around $n_e \approx 0.15 \times 10^{12}$ cm^{-2}.

The λ obtained for the topological superconductivity from a single, convex FS turned out to be relatively small [Fig. 5(a)]. This changes closer to the VHS, where the single contour FS takes on a flower shape (F contour in Fig. 2). As shown in Fig. 5(b), for the flower-shaped FS, λ grows rapidly with decreasing density. Thus, we observe that within the Kohn-Luttinger mechanism, the corrugated nature of the single-contour FS substantially enhances the superconducting coupling constant. Here the leading superconducting instability again has p-wave symmetry with a nonzero Chern number (cf. Appendix E). While λ rapidly increases with decreasing density, the appearance of the Stoner transition at higher densities [shaded region in Fig. 5(b)] in this case precludes the development of the dome-shaped superconducting region. Therefore, for large values of Δ_1, superconductivity is only limited to a narrow region adjacent to Stoner instability, similar to the ABC trilayer.

Overall, we find that the ABCA tetralayer is qualitatively different from the ABC trilayer since it gives rise to regions with robust topological superconductivity. In particular, the Kohn-Luttinger mechanism suggests a $p + ip$ topological superconducting phase immediately preceding the Stoner transition at large perpendicular electric fields, 58 meV $\leqslant \Delta_1 \leqslant 68$ meV. At even larger fields, the superconducting transition of the ABCA tetralayer for the conduction band should be similar to the ABC trilayer, with an annular-shaped FS and a topologically trivial superconducting state.

V. DISCUSSION

We investigated multilayer graphenes as potential candidates for realization of symmetry-broken phases and superconductivity, identifying tetralayer ABCA stacks of graphene as the most promising candidate for realizing interaction-driven physics. The dominant superconducting instability has a *p*-wave order parameter and typically occurs for the annular or pocket geometry of the FS. This is in line with the established intuition that the Kohn-Luttinger mechanism is enhanced in the presence of multipocket FSs [45,48]. According to our findings, the superconducting regions are expected to trail the Stoner transitions—a qualitative prediction that is testable in future experiments. Somewhat surprisingly, we also found significant superconducting instabilities for certain simply connected FSs that either have an approximate sixfold rotation symmetry or are severely corrugated (i.e., the FS has a flower shape). We predict that the superconducting phase resulting from such simply connected FSs is topological.

The topological superconducting phase will manifest itself with two topologically protected copropagating chiral edge modes originating from the two valleys. These edge states can be detected in tunneling experiments into the edges or through their quantized contribution to the thermal Hall conductivity of $\kappa_{XY} = \pi^2 k_B^2 C / (6h)$ [66], where C is the Chern number of the superconducting state.

We note that a scenario for (nontopological) superconductivity due to phonons has recently been proposed for displaced bilayer systems [67] and ABCA graphene [68]. In contrast to our results, the phonon mechanism for ABCA graphene predicts dome-shaped superconducting regions with *s*- or *f*-wave symmetry for a broad range of densities and for large values of the electric field. While we do find some regions with a dome-shaped superconducting instability, in our analysis the most robust superconducting states occur in narrow density ranges near the border between two phases with different patterns of valley and spin symmetry breaking. We note also that a setup for realizing topological superconductivity by combining two nontopological *f*-wave superconductors with a relative twist angle has been proposed recently [69].

Topological superconductivity from a singly connected FS is a distinct possibility that emerges only for tetralayer graphene. Conceptually, it suggests that the Kohn-Luttinger mechanism can give rise to a sizable instability also for the simply connected FSs, provided these are sufficiently far from a circular FS with parabolic dispersion. It would be interesting to study the Kohn-Luttinger scenario for other systems characterized by a strongly warped or distorted FS at strong Coulomb interactions, thus uncovering optimal conditions for superconductivity enhancement [49]. Independent of that, the approximate sixfold symmetry of the FS which we find in ABCA graphene is expected to occur in other multilayer two-dimensional materials with a hexagonal lattice. An accurate treatment of potential competing instabilities of such approximately nested FS remains an interesting open question.

To conclude, we reveal that despite its relative complexity, tetralayer graphene holds the promise of realizing new physics, including topological superconductivity, that was hitherto not observed in a graphene stacks with a smaller number of layers. Although we identified ABCA graphene as the most promising material, a large number of other potential systems remain beyond the scope of our paper. This applies, in particular, to uncoventional ABCB stacks, which have a relatively high DOS as well (cf. Appendix A) and which were recently realized experimentally [57]. In addition, our Stoner model did not include possible nematic phases that would break the threefold rotation symmetry of underlying graphene lattice. These phases are likely to occur in the regime of low density, when the FS typically contains several small pockets [70]. We hope that joint future theoretical and experimental studies will advance our understanding of interaction effects of multilayer graphenes, thereby facilitating the realization of new phases of matter.

APPENDIX A: TIGHT-BINDING MODEL FOR BAND STRUCTURE AND SCREENING

1. Bilayer and trilayer graphenes

To consider band structures of multilayer graphene, we adopt the standard Slonczewski-Weiss-McClure parametrization of the tight-binding model [60]. We retain hopping amplitudes effective up to three layers. Hopping structures and values used throughout this paper are shown in Fig. 6. The parameter values are adopted from Refs. [6,71]. In particular, since we are interested in ABCA stacking, we use the parameters proposed for ABC graphene [71]. For certain stackings, an additional hopping γ_5 is present (see Fig. 6), which is absent for ABC graphene. In this case, we adopt the value estimated for ABA graphene [71]. The band structure of bilayer and trilayer graphene has been considered before [6,10,72–75]. For completeness, we reproduce here the tight-binding Hamiltonian of the bilayer and trilayer. Denoting A_i and B_i for the different sublattice sites on layer i, for the bilayer the basis is (A_1, B_1, A_2, B_2) and we write

$$H_{\mathrm{BG}} = \begin{pmatrix} \Delta_1 & v_0\pi^{\dagger} & v_4\pi^{\dagger} & v_3\pi \\ v_0\pi & \Delta_1 + \delta & \gamma_1 & v_4\pi^{\dagger} \\ v_4\pi & \gamma_1 & -\Delta_1 + \delta & v_0\pi^{\dagger} \\ v_3\pi^{\dagger} & v_4\pi & v_0\pi & -\Delta_1 \end{pmatrix}, \quad \text{(A1)}$$

where $\pi = \tau k_x + i k_y$ (τ is the valley index) and $v_i = \sqrt{3}a\gamma_i/2$, $a = 2.46$ Å is the lattice constant of graphene. $2\Delta_1$ is the potential difference between the layers and is proportional to the perpendicular electric field and δ is the on-site potential for the sublattice sites which have a direct neighbor on the adjacent layer (see Fig. 6 for schematics and values of parameters). For the trilayer case, we have two stackings st = ABA and ABC, so we use the following parametrization:

$$H_{\mathrm{st}} = H_{\mathrm{st},0} + H_{\Delta_1} + H_{\Delta_2}, \quad \text{(A2)}$$

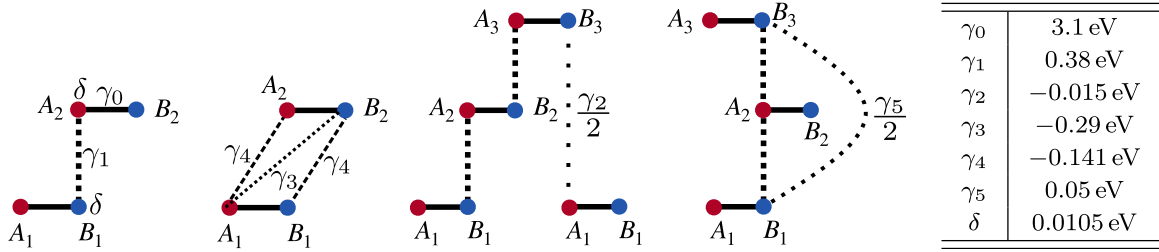|	
γ_0	3.1 eV
γ_1	0.38 eV
γ_2	-0.015 eV
γ_3	-0.29 eV
γ_4	-0.141 eV
γ_5	0.05 eV
δ	0.0105 eV

FIG. 6. Schematic representation of hopping and on-site parameters γ_i and δ (left) and corresponding values used in the current calculations (right).

with

$$H_{\mathrm{ABA},0} = \begin{pmatrix} 0 & v_0\pi^\dagger & v_4\pi^\dagger & v_3\pi & \frac{1}{2}\gamma_2 & 0 \\ v_0\pi & \delta & \gamma_1 & v_4\pi^\dagger & 0 & \frac{1}{2}\gamma_5 \\ v_4\pi & \gamma_1 & \delta & v_0\pi^\dagger & v_4\pi & \gamma_1 \\ v_3\pi^\dagger & v_4\pi & v_0\pi & 0 & v_3\pi^\dagger & v_4\pi \\ \frac{1}{2}\gamma_2 & 0 & v_4\pi^\dagger & v_3\pi & 0 & v_0\pi^\dagger \\ 0 & \frac{1}{2}\gamma_5 & \gamma_1 & v_4\pi^\dagger & v_0\pi & \delta \end{pmatrix}, \tag{A3}$$

$$H_{\mathrm{ABC},0} = \begin{pmatrix} 0 & v_0\pi^\dagger & v_4\pi^\dagger & v_3\pi & 0 & \frac{1}{2}\gamma_2 \\ v_0\pi & \delta & \gamma_1 & v_4\pi^\dagger & 0 & 0 \\ v_4\pi & \gamma_1 & \delta & v_0\pi^\dagger & v_4\pi^\dagger & v_3\pi \\ v_3\pi^\dagger & v_4\pi & v_0\pi & \delta & \gamma_1 & v_4\pi^\dagger \\ 0 & 0 & v_4\pi & \gamma_1 & \delta & v_0\pi^\dagger \\ \frac{1}{2}\gamma_2 & 0 & v_3\pi^\dagger & v_4\pi & v_0\pi & 0 \end{pmatrix}, \tag{A4}$$

$$H_{\Delta_1} = \mathrm{diag}(\Delta_1, \Delta_1, 0, 0, -\Delta_1, -\Delta_1), \tag{A5}$$

$$H_{\Delta_2} = \mathrm{diag}(\Delta_2, \Delta_2, -2\Delta_2, -2\Delta_2, \Delta_2, \Delta_2), \tag{A6}$$

where we have used $(A_1, B_1, A_2, B_2, A_3, B_3)$ as the basis. For this case, $2\Delta_1$ is the potential difference between outer layers and $3\Delta_2$ corresponds to the difference between the mean potential of the outer layers and the middle layer. For trilayer systems, we adopt the value $\Delta_2 = -0.0023$ eV.

2. Tetralayer graphenes

There are three possible energetically stable stackings of tetralayer graphene, st = ABCA, ABAB, and ABAC (or, equivalently, ABCB). Generally, we can write the Hamiltonian in the form

$$H_{\mathrm{st}} = H_{0,\mathrm{st}} + H_{\Delta_1} + H_{\Delta_2} + H_{\Delta_3}, \tag{A7}$$

where H_{Δ_1}, H_{Δ_2}, and H_{Δ_3} describe the electrostatic potentials on different layers and are independent of the stacking. In the basis $(A_1, B_1, A_2, B_2, A_3, B_3, A_4, B_4)$, they have the form

$$H_{\Delta_1} = \mathrm{diag}\left(\Delta_1, \Delta_1, \frac{\Delta_1}{3}, \frac{\Delta_1}{3}, -\frac{\Delta_1}{3}, -\frac{\Delta_1}{3}, -\Delta_1, -\Delta_1\right), \tag{A8}$$

$$H_{\Delta_2} = \mathrm{diag}(\Delta_2, \Delta_2, -\Delta_2, -\Delta_2, -\Delta_2, -\Delta_2, \Delta_2, \Delta_2), \tag{A9}$$

$$H_{\Delta_3} = \mathrm{diag}(0, 0, -\Delta_3, -\Delta_3, \Delta_3, \Delta_3, 0, 0). \tag{A10}$$

$H_{\mathrm{st},0}$ is the 8×8 Hamiltonian for each stacking case. They are written explicitly as

$$H_{\mathrm{ABCA},0} = \begin{pmatrix} 0 & v_0\pi^\dagger & v_4\pi^\dagger & v_3\pi & 0 & \frac{1}{2}\gamma_2 & 0 & 0 \\ v_0\pi & \delta & \gamma_1 & v_4\pi^\dagger & 0 & 0 & 0 & 0 \\ v_4\pi & \gamma_1 & \delta & v_0\pi^\dagger & v_4\pi^\dagger & v_3\pi & 0 & \frac{1}{2}\gamma_2 \\ v_3\pi^\dagger & v_4\pi & v_0\pi & \delta & \gamma_1 & v_4\pi^\dagger & 0 & 0 \\ 0 & 0 & v_4\pi & \gamma_1 & \delta & v_0\pi^\dagger & v_4\pi^\dagger & v_3\pi \\ \frac{1}{2}\gamma_2 & 0 & v_3\pi^\dagger & v_4\pi & v_0\pi & \delta & \gamma_1 & v_4\pi^\dagger \\ 0 & 0 & 0 & 0 & v_4\pi & \gamma_1 & \delta & v_0\pi^\dagger \\ 0 & 0 & \frac{1}{2}\gamma_2 & 0 & v_3\pi^\dagger & v_4\pi & v_0\pi & 0 \end{pmatrix}, \tag{A11}$$

$$H_{\mathrm{ABAB},0} = \begin{pmatrix} 0 & v_0\pi^\dagger & v_4\pi^\dagger & v_3\pi & \frac{1}{2}\gamma_2 & 0 & 0 & 0 \\ v_0\pi & \delta & \gamma_1 & v_4\pi^\dagger & 0 & \frac{1}{2}\gamma_5 & 0 & 0 \\ v_4\pi & \gamma_1 & \delta & v_0\pi^\dagger & v_4\pi & \gamma_1 & \frac{1}{2}\gamma_5 & 0 \\ v_3\pi^\dagger & v_4\pi & v_0\pi & 0 & v_3\pi^\dagger & v_4\pi & 0 & \frac{1}{2}\gamma_2 \\ \frac{1}{2}\gamma_2 & 0 & v_4\pi^\dagger & v_3\pi & 0 & v_0\pi^\dagger & v_4\pi^\dagger & v_3\pi \\ 0 & \frac{1}{2}\gamma_5 & \gamma_1 & v_4\pi^\dagger & v_0\pi & \delta & \gamma_1 & v_4\pi^\dagger \\ 0 & 0 & \frac{1}{2}\gamma_5 & 0 & v_4\pi & \gamma_1 & \delta & v_0\pi^\dagger \\ 0 & 0 & 0 & \frac{1}{2}\gamma_2 & v_3\pi^\dagger & v_4\pi & v_0\pi & 0 \end{pmatrix}, \tag{A12}$$

$$
H_{\text{ABAC},0} = \begin{pmatrix}
0 & v_0\pi^\dagger & v_4\pi^\dagger & v_3\pi & \frac{1}{2}\gamma_2 & 0 & 0 & 0 \\
v_0\pi & \delta & \gamma_1 & v_4\pi^\dagger & 0 & \frac{1}{2}\gamma_5 & 0 & 0 \\
v_4\pi & \gamma_1 & \delta & v_0\pi^\dagger & v_4\pi & \gamma_1 & 0 & 0 \\
v_3\pi^\dagger & v_4\pi & v_0\pi & 0 & v_3\pi^\dagger & v_4\pi & \frac{1}{2}\gamma_2 & 0 \\
\frac{1}{2}\gamma_2 & 0 & v_4\pi^\dagger & v_3\pi & \delta & v_0\pi^\dagger & v_4\pi & \gamma_1 \\
0 & \frac{1}{2}\gamma_5 & \gamma_1 & v_4\pi^\dagger & v_0\pi & \delta & v_3\pi^\dagger & v_4\pi \\
0 & 0 & 0 & \frac{1}{2}\gamma_2 & v_4\pi^\dagger & v_3\pi & 0 & v_0\pi^\dagger \\
0 & 0 & 0 & 0 & \gamma_1 & v_4\pi^\dagger & v_0\pi & \delta
\end{pmatrix}.
\tag{A13}
$$

In all calculations, we choose $\Delta_2 = \Delta_3 = 0$, since those are supposed to be in a range of few meV (see the discussion of the screening below) and will not have an important effect on the conclusions of the paper.

3. Band structure of ABCAB graphene

In Fig. 7, we compare the DOS for ABCA tetralayer with ABCAB pentalayer. While for $\Delta_1 = 0$ (generally for $\Delta_1 < 10$ meV), the additional layer gives some enhancement of the DOS, for larger values of Δ_1, the tetralayer has a comparable or even larger DOS compared to the pentalayer. Due to the low-lying additional bands in the latter, screening is expected to be stronger for the pentalayer than for the tetralayer, narrowing the experimentally accessible window in which the asymmetry potential can be tuned. Therefore, adding more layers ceases to be helpful beyond four layers, which is why we concentrate on systems with up to four layers in the main text.

4. Band structure of ABAC/ABCB graphene

In the family of multilayer graphene stackings up to four layers, ABCB plays a special role since it both lacks an inversion center and mirror symmetry [cf. Fig. 8(a)]. Therefore, its band structure depends on the sign of the potential Δ_1. This is shown in Figs. 8(b) and 8(c). For $\Delta_1 = 0$, the band structure is gapless and remains such also for negative $\Delta_1 < 0$, at least up to $\Delta_1 = -60$ meV [cf. Fig. 8(c)]. It should be mentioned that there is no symmetry protecting the band crossing for $\Delta_1 < 0$. Figures 8(d) and 8(e) compares the DOS for ABCB and ABCA stackings. For the chosen tight-binding parameters, ABCA has a higher DOS for all values of the asymmetry potential. Therefore, we expect interaction effects and superconducting instabilities to be less pronounced in ABCB graphene compared to ABCA.

5. Low-energy band structure of ABCA graphene

Since in the remainder of our paper we focus on ABCA stacking, we derive the low-energy Hamiltonian corresponding to A_1 and B_4 sublattices. Following the standard procedure
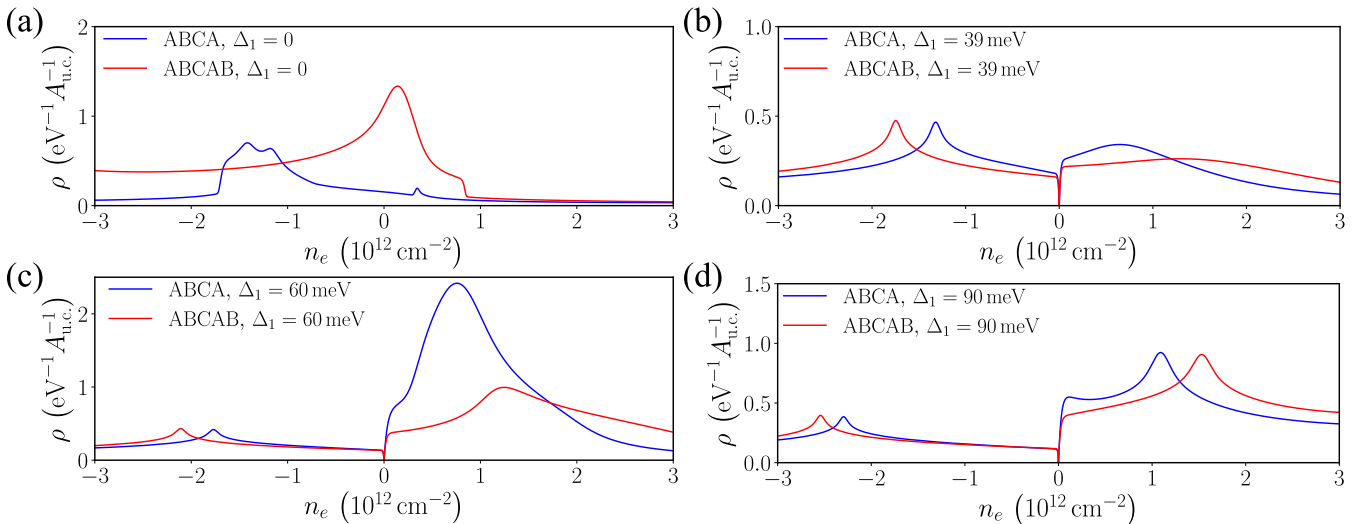

FIG. 7. Comparison of the DOS for tetralayer ABCA and pentalayer ABCAB for different values of the layer asymmetry potential. While for $\Delta_1 = 0$ ABCAB graphene has a higher DOS, at other values of the displacement field the DOS of ABCA is comparable or larger.
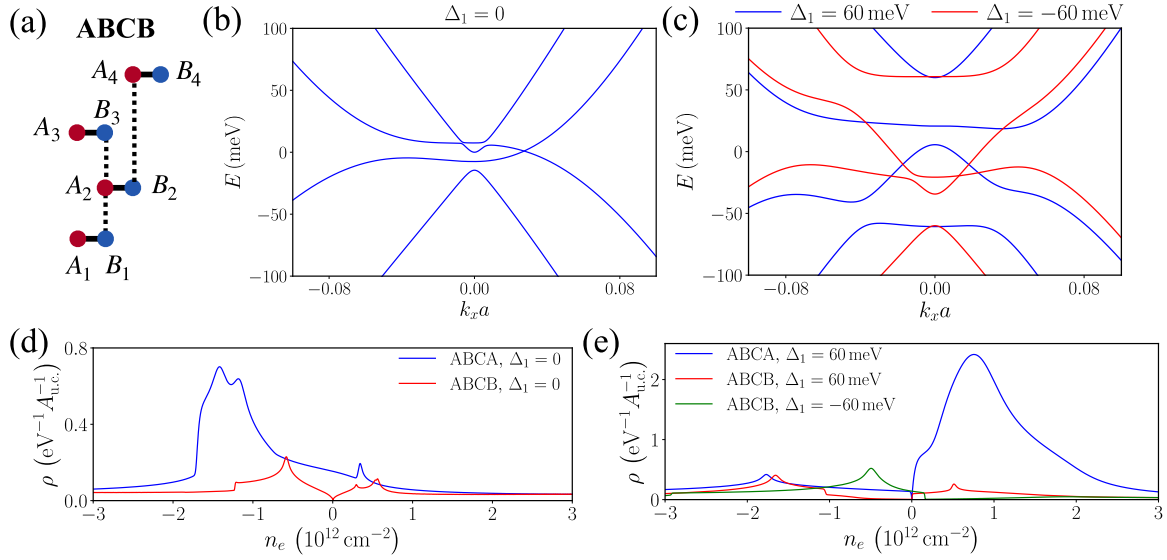
FIG. 8. Stacking order (a) and energy dispersion (b), (c) for ABCB graphene with zero and nonzero displacement field Δ_1. (d), (e) Comparison of the corresponding DOS of ABCB and ABCA stackings. Note the dependence of the band structure and DOS of ABCB graphene on the sign of Δ_1.

[73], we get

$$
h_{\text{eff}}(\mathbf{k}) = -\delta \frac{v_0^2 k^2}{\gamma_1^2} \sigma_0 + \Delta_2 \sigma_0 + \Delta_1 \left(1 + \frac{4v_0^2 k^2}{3\gamma_1^2} \right) \sigma_z - \Delta_3 \frac{v_0^2 k^2}{\gamma_1^2} \sigma_z
$$

$$
- \underbrace{\frac{v_0^4 k^4}{\gamma_1^3} (\cos(4\varphi_{\mathbf{k}}) \sigma_x + \tau \sin(4\varphi_{\mathbf{k}}) \sigma_y)}_{\text{BP4}} - \frac{2v_0 v_4 k^2}{\gamma_1} \sigma_0 - \underbrace{\frac{v_3^2 k^2}{\gamma_1} (\cos(2\varphi_{\mathbf{k}}) \sigma_x - \tau \sin(2\varphi_{\mathbf{k}}) \sigma_y)}_{\text{BP2}}
$$

$$
+ \underbrace{\left(\frac{2v_0 v_3 v_4 \tau}{\gamma_1^2} - \frac{v_0^2 v_4 \gamma_2 \tau}{\gamma_1^3} \right) (k_x^3 - 3k_x k_y^2) \sigma_0}_{\text{BP0}} + \underbrace{\left(\frac{3v_0^2 v_3 k^3}{\gamma_1^2} - \frac{v_0^3 \gamma_2 k^3}{\gamma_1^3} - \frac{v_0 \gamma_2 k}{\gamma_1} \right) (\tau \cos \varphi_{\mathbf{k}} \sigma_x + \sin \varphi_{\mathbf{k}} \sigma_y)}_{\text{BP1}}, \quad \text{(A14)}
$$

where $\tau = \pm 1$ is the valley index and we assumed $\gamma_2 \ll \gamma_1$ and kept only v_3/γ_1 and v_4/γ_1 terms up to first order.

Figure 9 shows the progression of the energy levels with the change of asymmetry potential Δ_1 and comparing the results from 8×8 Hamiltonian Eq. (A7) and from effective Hamiltonian Eq. (A14). As shown in the main text, a nonzero asymmetry potential opens a gap. For small values of Δ_1, the electron band has a single FS and for those cases the effective Hamiltonian Eq. (A14) captures the main features quite well. For higher values of Δ_1 and at $n_e > -3 \times 10^{12}$ cm^{-2} charge densities of the hole band, the FS consists of three pockets or an annulus. For those cases, the effective 2×2 model is less useful since it is an expansion of an 8×8 Hamiltonian that relies on k being a small parameter.

In the Hamiltonian Eq. (A14), we observe the presence of the terms with Berry phase equal to 4, 2, and 1 denoted as BP4, BP2, and BP1, respectively. The last line of Eq. (A14) also contains a term (denoted as BP0) which causes additional trigonal warping of the FS and is proportional to the identity matrix in sublattice space, σ_0. For the current values of tight-binding parameters, this term gives a small contribution and we do not consider it further. Figure 10 shows the change of the FS of the electronic band as different terms in Eq. (A14)

are set to zero. For the case of BP1 $= 0$ and BP2 $= 0$, the FS becomes circular. A nonzero BP2 term results in a *six-fold* warping of the surface, so it becomes reminiscent of a hexagon shape. Finally, the term with the Berry phase equal to one (BP1) leads to trigonal warping. Since BP1 contains contributions of order k and k^3 with opposite signs, at a certain value of the density these two contributions cancel each other. Therefore, upon changing the carrier density it is possible to flip the *orientation* of the trigonal warping. To the best of our knowledge, this is the unique feature of the tetralayer that does not appear in mono-, bi-, or trilayer graphenes.

6. Screening in tetralayer ABCA graphene

To determine the experimentally accessible range of Δ_1 and the values of Δ_2 and Δ_3, we consider the self-consistent Hartree screening due to the presence of gates [76]. Denoting the layer potentials as u_i, we define the Δ_i parameters for tetralayer graphene stacks as

$$
\Delta_1 = \frac{u_1 - u_4}{2}, \quad \text{(A15)}
$$

$$
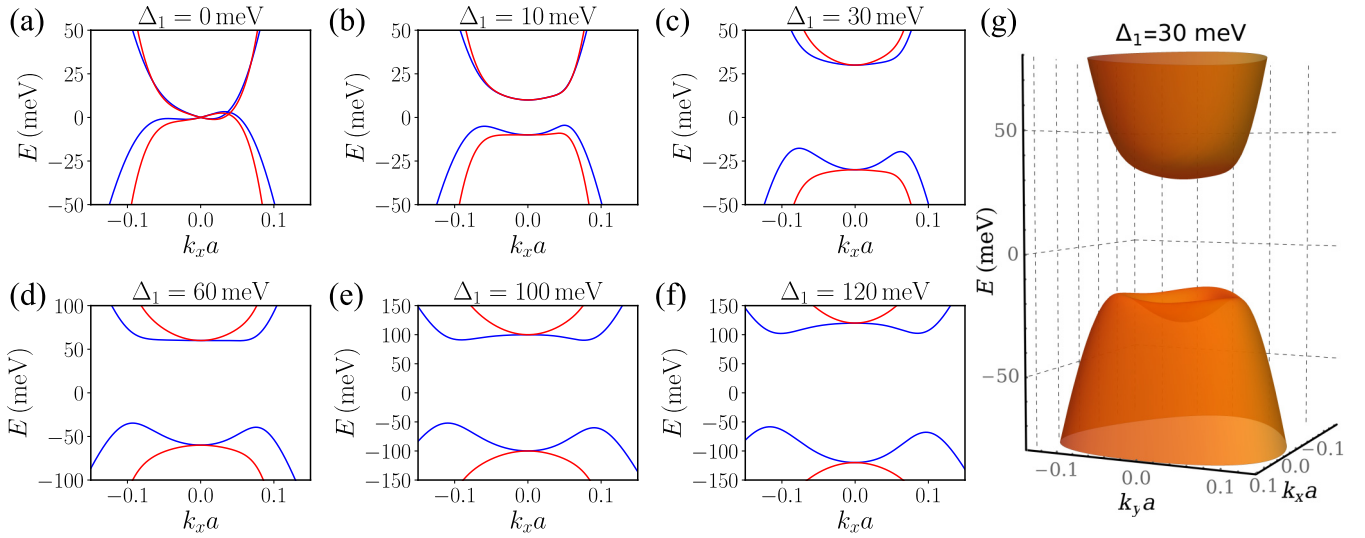\Delta_2 = \frac{u_1 - u_2 - u_3 + u_4}{4}, \quad \text{(A16)}
$$

FIG. 9. (a)–(f) Progression of the energy bands of ABCA graphene as a function of $k_x a$ with the change of the asymmetry potential Δ_1. Blue (red) lines are from Hamiltonian Eq. (A7) [effective Hamiltonian Eq. (A14)]. (g) 3D plot of the energy bands for $\Delta_1 = 30$ meV from Hamiltonian Eq. (A7).

$$\Delta_3 = \frac{u_1 - 3u_2 + 3u_3 - u_4}{6}. \quad \text{(A17)}$$

Assuming that average potential in the graphene multilayer is zero yields the constraint $u_1 + u_2 + u_3 + u_4 = 0$. Then, using standard electrostatics we can relate Δ_i to the potential on the gates and the charge densities n_i at each layer:

$$\Delta_1 = \frac{3}{4}\frac{ed}{\epsilon_r}\left(\frac{\epsilon_t V_t}{L_t} - \frac{\epsilon_b V_b}{L_b}\right) + \frac{e^2 d}{4\epsilon_r}[3(n_1 - n_4) + (n_2 - n_3)], \quad \text{(A18)}$$

$$\Delta_2 = -\frac{e^2 d}{4\epsilon_r}(n_2 + n_3), \quad \text{(A19)}$$

$$\Delta_3 = -\frac{e^2 d}{6\epsilon_r}(n_2 - n_3). \quad \text{(A20)}$$

Here $d = 3.34$ Å is the distance between the layers, while V_t (V_b) is the potential on the top (bottom) gate, L_t (L_b) are the distances between the top (bottom) gate, and the graphene sample, while likewise ϵ_t (ϵ_b) are the dielectric constants between top (bottom) gate and the graphene sample. Identifying $\Delta_{1,\text{ext}} = \frac{3}{4}\frac{ed}{\epsilon_r}\left(\frac{\epsilon_t V_t}{L_t} - \frac{\epsilon_b V_b}{L_b}\right)$ as the external potential, we arrive at a system of equations that can be solved self-consistently,

yielding an estimate of the external potentials accessible in experiment. For concreteness, we fix the dielectric constant that does not take into account self-consistent screening as $\epsilon_r = 2$. The value of this constant is smaller compared to the value of $\epsilon = 4$ in the main text, but the effective screening is enhanced due to screening from itinerant charge degrees of freedom. The displacement field is defined as $D = \frac{\epsilon_t V_t}{L_t} - \frac{\epsilon_b V_b}{L_b}$ [71]. In experiment, the upper limit of D is typically in the order of $D_{\max} = 2.0$ V/nm, which yields $\Delta_{1,\text{ext}}^{\max} \approx 250$ meV.

Figure 11 shows the dependence of the Δ_1, Δ_2, and Δ_3 potentials on external potential $\Delta_{1,\text{ext}}$ as calculated from self-consistent Hartree screening. Note that this calculation requires knowledge of the charge-density distribution between layers. This has a contribution from all momenta in the Brillouin zone and, therefore, a full zone sampling is necessary. As can be seen from the figure, Δ_2 and Δ_3 are in the range of a few meV and can be safely set to zero, since that range does not have a noticeable effect on the band structure. Taking into account the effect of the screening and using the maximum value of the external potential, Δ_1 can take values up to $100-120$ meV, which exceeds any of the displacement field parameters discussed in the main text by a fair margin. Therefore, we expect that all the effects
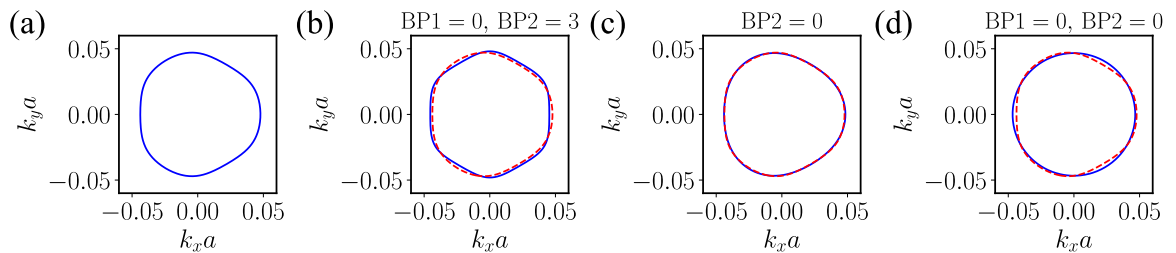

FIG. 10. Fermi surfaces of ABCA graphene for $\Delta_1 = 9$ meV and $n = 1.1 \times 10^{12}$ cm^{-2} obtained from the effective Hamiltonian Eq. (A14) is shown in (a). All subsequent panels illustrate the change of the FS when specific terms in effective Hamiltonian are set to zero. In (b), BP2 = 3 title means the BP2 term was magnified three times to make the effect of the term more pronounced. When BP1 = 0, BP2 causes sixfold warping of the Fermi surface. In contrast, BP1 causes trigonal warping (c). When both BP1 = 0 and BP2 = 0, the Fermi surface is circular (d). In (b)–(d), red dashed lines show the FS from (a) for comparison.
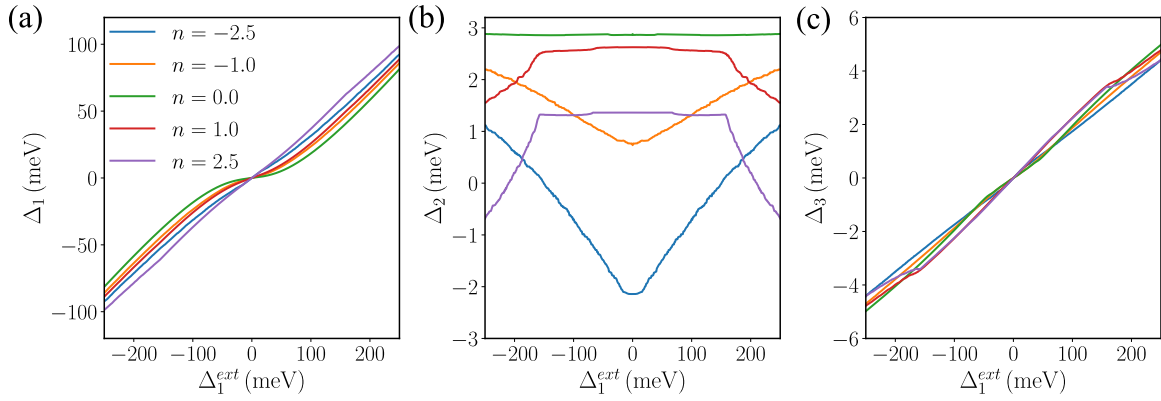
FIG. 11. Dependence of Δ_1 (a), Δ_2 (b), and Δ_3 (c) parameters for ABCA graphene on external layer asymmetry potential $\Delta_{1,\text{ext}}$ determined from self-consistent Hartree screening. The calculation employs 1000×1000 grid points from full Brillouin zone. Densities are given in units of 10^{12} cm^{-2}.

described in this paper can be observed with presently available methods.

APPENDIX B: FERMIOLOGY OF ABCA GRAPHENE

In this Appendix, we discuss the high DOS region on the electron side where several VHSs meet. This leads to a higher order VHS, similar to the one discussed in the context of twisted bilayer graphene [77]. The resulting DOS as a function of Δ_1 and n is shown in Fig. 12, alongside with a few representative FSs which emerge. The fermiology is very rich in a narrow region of densities and displacement fields in the vicinity of the higher order VHS. At the higher order VHS, where five conventional VHSs nearly collide, we observe three FSs originating from the same band. There are also regions with four pockets with different topologies. The divergence of the DOS is higher than at the individual VHS

and interaction effects are expected to be dominant. In the Stoner interaction model considered in the main text (cf. next section), the system gets strongly polarized and such FSs are only observed in the region of the phase diagram with full spin and valley polarization (1x degenerate).

APPENDIX C: STONER TRANSITIONS

As for the case of trilayer graphene [6], Stoner transitions are obtained through the minimization of the grand potential density

$$\frac{\Phi}{A} = \sum_\alpha E_0(n_\alpha) + V_{\text{int}} - \mu \sum_\alpha n_\alpha, \quad \text{(C1)}$$

where E_0 is the kinetic energy and n_α is density of each flavor corresponding to spin and valley. V_{int} is the interaction potential, which besides a SU(4) symmetric term also includes the scattering between valleys, namely,

$$V_{\text{int}} = \frac{U A_{\text{u.c.}}}{2} \sum_{\alpha \neq \beta} n_\alpha n_\beta + J A_{\text{u.c.}}(n_1 - n_3)(n_2 - n_4), \quad \text{(C2)}$$

where we used the indexing $1 = \{K, \uparrow\}$, $2 = \{K', \uparrow\}$, $3 = \{K, \downarrow\}$, $4 = \{K', \downarrow\}$ and $A_{\text{u.c.}} = \sqrt{3}a^2/2$ is the area of unit cell. Here U and J are the interaction constants at the unit cell level. For ABC trilayer parameter values $U = 30$ eV and $J = -9$ eV has been used [6]. We show the Stoner phase diagram for ABCA tetralayer in Fig. 13. Due to the larger number of layers, we expect the strength of U and J to be
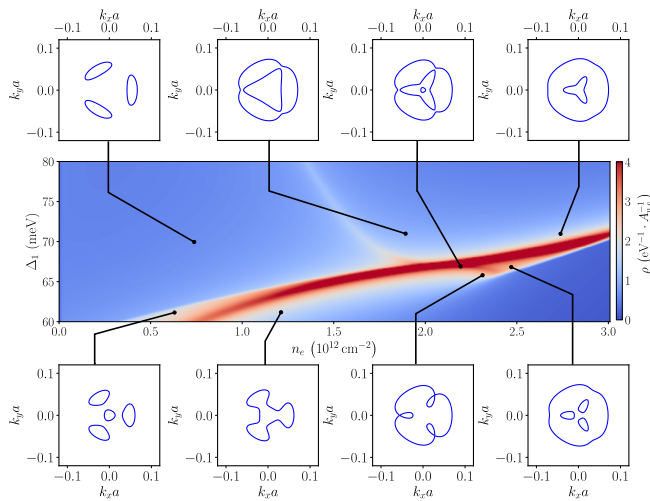

FIG. 12. Color plot of the DOS ρ for the ABCA tetralayer, similar to Fig. 2 in the main text but zoomed in for large displacement field on the electron side. In this region of the phase diagram, several VHSs occur in close proximity. Representative Fermi surfaces are shown for selected locations, some of which appear only close to these Lifshitz points and not anywhere else in the phase diagram.
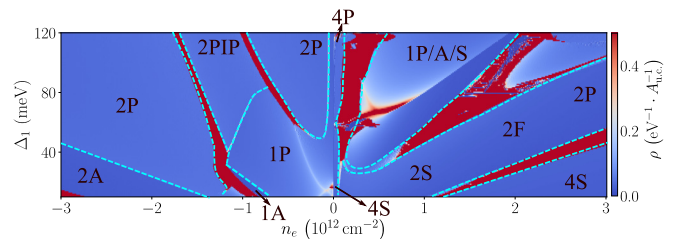

FIG. 13. Stoner phase diagram for interaction strengths $U = 30$ eV and $J = -9$ eV. The labels are the same as in the Stoner diagram (Fig. 3) of the main text.
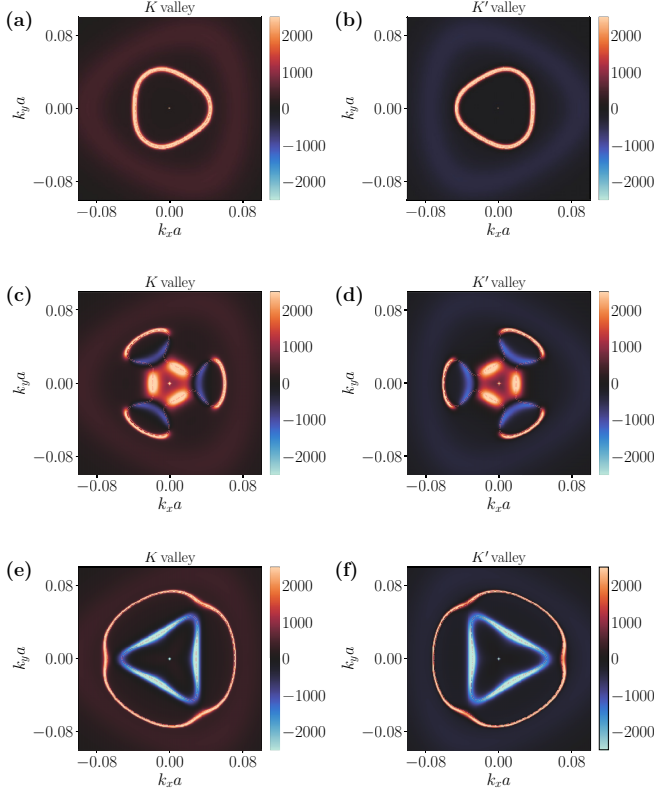
FIG. 14. (a)-(b) Berry curvature obtained from BdG equations for ABCA stacking assuming $p_x + ip_y$ pairing in the electronic band for $\Delta_1 = 42$ meV, $\mu = 43.4$ meV, and $\Delta_p = 0.1$ meV. Red dashed lines show the Fermi surface of the parent Hamiltonian. The Chern number due to the superconducting pairing is 1 for both valleys. (c)-(d) The same as in top panel but for $\Delta_1 = 60$ meV and $\mu = 60.08$ meV. The Chern number due to the superconducting pairing is 1 for both valleys. (e)-(f) The same as in top panels but for $\Delta_1 = 69$ meV and $\mu = 68.77$ meV. The Chern number due to the superconducting pairing is 0 for both valleys.

weaker for tetralayer compared to trilayer graphene. Therefore, in the main text we show a Stoner phase diagram for $U = 15$ eV and $J = -4.5$ eV. Comparing the two diagrams, we see qualitatively similar phases. The triple degenerate phase is absent in both cases. For weaker interaction strength, the so-called PIP phases that are characterized by unequal population of different flavors are more prevalent. More importantly, for weaker values of the interaction, the fourfold degenerate phase on the electron side spans a broader range of densities and asymmetry potential, thereby also pushing the double degenerate phase to higher Δ_1 and lower n. Since the electronic mechanism for superconductivity which we consider in this paper only yields topological superconductivity from a double degenerate parent phase, weaker values of the interaction are therefore more favorable toward realizing topological superconductivity.

Finally, let us comment on the magnitude of the values U and J chosen above in comparison to the scale of Coulomb interaction used to determine the superconducting instability. The interaction parameter Ua^2 in the Stoner model, where a is the graphene lattice spacing, is expected to be comparable to the screened Coulomb interaction at wave vector q of the

order of k_F, which represents the typical momentum transfer entering the exchange interaction. Since, typically a FS is multipocket, it is not clear which of the different k_F present in the problem to choose. Nevertheless, for an order of magnitude estimate, we use the average k_F of the different Fermi pockets at a representative density and displacement field. Taking the density $n = 2 \times 10^{12}$ cm^{-2} and estimating $k_F = 0.035$ Å^{-1}, we obtain for U, $U \propto \frac{1}{A_{\text{u.c.}}} \frac{2\pi e^2}{\epsilon(2k_F)}$, where we use the area of the unit cell $A_{\text{u.c.}} = \sqrt{3}a^2/2 \approx 5$ Å^2 with $a = 0.24$ nm. Substituting the value of k_F, we obtain $U \propto \frac{18}{\epsilon} \times 13.6$ eV, which for $\epsilon = 4$ gives $U \propto 60$ eV, which is of the same order of magnitude of the values of U used in this paper.

APPENDIX D: LEADING SUPERCONDUCTING INSTABILITIES

We investigate the superconducting instabilities driven by the long-range Coulomb interaction. To this end, the effective interaction between electrons is calculated incorporating particle-hole fluctuations through the RPA [36]. The interaction potential is then given by

$$V_{\boldsymbol{q}} = \frac{V_{0,\boldsymbol{q}}}{1 + \Pi_{0,\boldsymbol{q}} V_{0,\boldsymbol{q}}}, \tag{D1}$$

and the effective interaction is treated as instantaneous. Here $V_{0,\boldsymbol{q}} = \frac{2\pi e^2}{\epsilon q} \tanh(qd)$ is the screened Coulomb interaction and

$$\Pi_{0,\boldsymbol{q}} = N \sum_{\boldsymbol{k}} |\Lambda_{\boldsymbol{k},\boldsymbol{q},\tau}|^2 \frac{f(\varepsilon_{\boldsymbol{k},\tau}) - f(\varepsilon_{\boldsymbol{k}+\boldsymbol{q},\tau})}{\varepsilon_{\boldsymbol{k}+\boldsymbol{q},\tau} - \varepsilon_{\boldsymbol{k},\tau}}$$

is the static polarization function, where N defines flavor degeneracy, $\varepsilon_{\boldsymbol{k},\tau}$ is the energy of the electron in valley τ, $f(x)$ is the Fermi-Dirac distribution, and $\Lambda_{\boldsymbol{k},\boldsymbol{q},\tau} = \langle u_{\boldsymbol{k},\tau} | u_{\boldsymbol{k}+\boldsymbol{q},\tau} \rangle$ is the overlap matrix element between states of the electron band at momenta $\boldsymbol{k}$ and $\boldsymbol{k} + \boldsymbol{q}$. Given the interaction potential $V_{\boldsymbol{q}}$, the superconducting instability can be determined by solving the linearized BCS gap equation with a linear operator

$$[\mathcal{M}\Delta]_{\boldsymbol{k}} = -\int \frac{dk'_{\parallel}}{(2\pi)^2 v_{k'}} V_{\boldsymbol{k}-\boldsymbol{k}'} |\Lambda_{\boldsymbol{k},\boldsymbol{k}'-\boldsymbol{k},+1}|^2 \Delta_{\boldsymbol{k}'}, \tag{D2}$$

where the integral is projected onto FS, $v_{\boldsymbol{k}}$ is the Fermi velocity, and $\Delta_{\boldsymbol{k}}$ is the order parameter to be determined. The calculation proceeds by discretizing (D2) and solving the eigenvalue matrix equation $\mathcal{M}_{\boldsymbol{k},\boldsymbol{k}'} \phi_{\boldsymbol{k}'} = \lambda \phi_{\boldsymbol{k}}$ [36].

APPENDIX E: TOPOLOGICAL SUPERCONDUCTIVITY

As is noted in the main text, for some range of parameters we obtain a superconducting instability with p-wave symmetry from the solution of the linearized gap equation. Based on general thermodynamic arguments [36], one can conclude that a system with C_3 symmetry favors chiral $p_x + ip_y$-type pairing below T_c. This reasoning applies directly to the case of the ABCA tetralayer, which has C_3 symmetry. This raises the interesting possibility that the resulting phase may be a topological superconductor. We address this question by calculating the Chern number due to the superconducting pairing for three representative cases of the FS topology.

To this end, we construct the Bogoliubov–de Gennes (BdG) Hamiltonian for the order parameter $\Delta_{\boldsymbol{k}} = \Delta_p(k_x +$

$ik_y)/k$. Once the energies and wave functions of the BdG equation are determined, the Berry curvature is calculated in a discretized Brillouin zone through the method of link variables [78]. Figure 14 shows the Berry curvature for three different FSs for which the stability analysis yielded p-wave pairing. Integrating the Berry curvature near K and K' valleys shows that the Chern number due to the superconducting pairing is 1 for each valley when the FS consists of a single

pocket. Therefore, both the top and middle panels in Fig. 14 correspond to topological superconductors with a total Chern number equal 2. In contrast, for an annular FS the Berry curvature near two Fermi surface contours has an opposite sign and the overall Chern number is zero (cf. bottom panel in Fig. 14). Therefore, for an annular Fermi surface, the resulting superconducting state is topologically trivial despite having a chiral $p_x + ip_y$ order parameter.

[1] Y. Cao, V. Fatemi, A. Demir, S. Fang, S. L. Tomarken, J. Y. Luo, J. D. Sanchez-Yamagishi, K. Watanabe, T. Taniguchi, E. Kaxiras *et al.*, Correlated insulator behaviour at half-filling in magic-angle graphene superlattices, Nature **556**, 80 (2018).

[2] Y. Cao, V. Fatemi, S. Fang, K. Watanabe, T. Taniguchi, E. Kaxiras, and P. Jarillo-Herrero, Unconventional superconductivity in magic-angle graphene superlattices, Nature **556**, 43 (2018).

[3] L. Balents, C. R. Dean, D. K. Efetov, and A. F. Young, Superconductivity and strong correlations in moiré flat bands, Nat. Phys. **16**, 725 (2020).

[4] J. M. Park, Y. Cao, K. Watanabe, T. Taniguchi, and P. Jarillo-Herrero, Tunable strongly coupled superconductivity in magic-angle twisted trilayer graphene, Nature **590**, 249 (2021).

[5] J. M. Park, Y. Cao, L. Xia, S. Sun, K. Watanabe, T. Taniguchi, and P. Jarillo-Herrero, Magic-angle multilayer graphene: A robust family of Moiré superconductors, Nat Mater. **21**(8), 877 (2022).

[6] H. Zhou, T. Xie, A. Ghazaryan, T. Holder, J. R. Ehrets, E. M. Spanton, T. Taniguchi, K. Watanabe, E. Berg, M. Serbyn, and A. F. Young, Half and quarter metals in rhombohedral trilayer graphene, Nature **598**, 429 (2021).

[7] H. Zhou, T. Xie, T. Taniguchi, K. Watanabe, and A. F. Young, Superconductivity in rhombohedral trilayer graphene, Nature **598**, 434 (2021).

[8] H. Zhou, L. Holleis, Y. Saito, L. Cohen, W. Huynh, C. L. Patterson, F. Yang, T. Taniguchi, K. Watanabe, and A. F. Young, Isospin magnetism and spin-polarized superconductivity in Bernal bilayer graphene, Science **375**, 774 (2022).

[9] Y. Zhang, R. Polski, A. Thomson, É. Lantagne-Hurtubise, C. Lewandowski, H. Zhou, K. Watanabe, T. Taniguchi, J. Alicea, and S. Nadj-Perge, Spin-orbit enhanced superconductivity in Bernal bilayer graphene, arXiv:2205.05087.

[10] E. McCann and M. Koshino, The electronic properties of bilayer graphene, Rep. Prog. Phys. **76**, 056503 (2013).

[11] E. V. Castro, N. M. R. Peres, T. Stauber, and N. A. P. Silva, Low-Density Ferromagnetism in Biased Bilayer Graphene, Phys. Rev. Lett. **100**, 186803 (2008).

[12] X.-F. Wang and T. Chakraborty, Coulomb screening and collective excitations in a graphene bilayer, Phys. Rev. B **75**, 041404(R) (2007).

[13] O. Vafek, Interacting fermions on the honeycomb bilayer: From weak to strong coupling, Phys. Rev. B **82**, 205106 (2010).

[14] F. Zhang, H. Min, M. Polini, and A. H. MacDonald, Spontaneous inversion symmetry breaking in graphene bilayers, Phys. Rev. B **81**, 041402(R) (2010).

[15] J. Jung, F. Zhang, and A. H. MacDonald, Lattice theory of pseudospin ferromagnetism in bilayer graphene: Competing

interaction-induced quantum Hall states, Phys. Rev. B **83**, 115408 (2011).

[16] M. F. Craciun, S. Russo, M. Yamamoto, J. B. Oostinga, A. F. Morpurgo, and S. Tarucha, Trilayer graphene is a semimetal with a gate-tunable band overlap, Nat. Nanotechnol. **4**, 383 (2009).

[17] A. Kumar, W. Escoffier, J. M. Poumirol, C. Faugeras, D. P. Arovas, M. M. Fogler, F. Guinea, S. Roche, M. Goiran, and B. Raquet, Integer Quantum Hall Effect in Trilayer Graphene, Phys. Rev. Lett. **107**, 126806 (2011).

[18] T. Taychatanapat, K. Watanabe, T. Taniguchi, and P. Jarillo-Herrero, Quantum Hall effect and Landau-level crossing of Dirac fermions in trilayer graphene, Nat. Phys. **7**, 621 (2011).

[19] Y. Lee, J. Velasco Jr, D. Tran, F. Zhang, W. Bao, L. Jing, K. Myhro, D. Smirnov, and C. N. Lau, Broken symmetry quantum Hall states in dual-gated ABA trilayer graphene, Nano Lett. **13**, 1627 (2013).

[20] L. C. Campos, T. Taychatanapat, M. Serbyn, K. Surakitbovorn, K. Watanabe, T. Taniguchi, D. A. Abanin, and P. Jarillo-Herrero, Landau Level Splittings, Phase Transitions, and Nonuniform Charge Distribution in Trilayer Graphene, Phys. Rev. Lett. **117**, 066601 (2016).

[21] A. L. Grushina, D.-K. Ki, M. Koshino, A. A. L. Nicolet, C. Faugeras, E. McCann, M. Potemski, and A. F. Morpurgo, Insulating state in tetralayers reveals an even–odd interaction effect in multilayer graphene, Nat. Commun. **6**, 6419 (2015).

[22] Z. Wu, Y. Han, J. Lin, W. Zhu, M. He, S. Xu, X. Chen, H. Lu, W. Ye, T. Han, Y. Wu, G. Long, J. Shen, R. Huang, L. Wang, Y. He, Y. Cai, R. Lortz, D. Su, and N. Wang, Detection of interlayer interaction in few-layer graphene, Phys. Rev. B **92**, 075408 (2015).

[23] Y. Shi, S. Che, K. Zhou, S. Ge, Z. Pi, T. Espiritu, T. Taniguchi, K. Watanabe, Y. Barlas, R. Lake, and C. N. Lau, Tunable Lifshitz Transitions and Multiband Transport in Tetralayer Graphene, Phys. Rev. Lett. **120**, 096802 (2018).

[24] S. Che, Y. Shi, J. Yang, H. Tian, R. Chen, T. Taniguchi, K. Watanabe, D. Smirnov, C. N. Lau, E. Shimshoni, G. Murthy, and H. A. Fertig, Helical Edge States and Quantum Phase Transitions in Tetralayer Graphene, Phys. Rev. Lett. **125**, 036803 (2020).

[25] Y. Nam, D.-K. Kl, D. Soler-Delgado, and A. F. Morpurgo, A family of finite-temperature electronic phase transitions in graphene multilayers, Science **362**, 324 (2018).

[26] Y. Lee, D. Tran, K. Myhro, J. Velasco, N. Gillgren, C. N. Lau, Y. Barlas, J. M. Poumirol, D. Smirnov, and F. Guinea, Competition between spontaneous symmetry breaking and single-particle gaps in trilayer graphene, Nat. Commun. **5**, 5656 (2014).

[27] K. Myhro, S. Che, Y. Shi, Y. Lee, K. Thilahar, K. Bleich, D. Smirnov, and C. N. Lau, Large tunable intrinsic gap in

rhombohedral-stacked tetralayer graphene at half filling, 2D Mater. **5**, 045013 (2018).

[28] A. Kerelsky, C. Rubio-Verdú, L. Xian, D. M. Kennes, D. Halbertal, N. Finney, L. Song, S. Turkel, L. Wang, K. Watanabe, T. Taniguchi, J. Hone, C. Dean, D. N. Basov, A. Rubio, and A. N. Pasupathy, Moiréless correlations in ABCA graphene, Proc. Natl. Acad. Sci. **118**, e2017366118(2021).

[29] Y. Lee, S. Che, J. Velasco, Jairo, D. Tran, J. Baima, F. Mauri, M. Calandra, M. Bockrath, and C. N. Lau, Gate tunable magnetism and giant magnetoresistance in ABC-stacked few-layer graphene, Nano Lett. **22**, 5094 (2022).

[30] Y. Shi, S. Xu, Y. Yang, S. Slizovskiy, S. V. Morozov, S.-K. Son, S. Ozdemir, C. Mullan, J. Barrier, J. Yin, A. I. Berdyugin, B. A. Piot, T. Taniguchi, K. Watanabe, V. I. Fal'ko, K. S. Novoselov, A. K. Geim, and A. Mishchenko, Electronic phase separation in multilayer rhombohedral graphite, Nature **584**, 210 (2020).

[31] H. Min and A. H. MacDonald, Electronic structure of multilayer graphene, Prog. Theor. Phys. Suppl. **176**, 227 (2008).

[32] F. Zhang, J. Jung, G. A. Fiete, Q. Niu, and A. H. MacDonald, Spontaneous Quantum Hall States in Chirally Stacked Few-Layer Graphene Systems, Phys. Rev. Lett. **106**, 156801 (2011).

[33] M. Otani, M. Koshino, Y. Takagi, and S. Okada, Intrinsic magnetic moment on (0001) surfaces of rhombohedral graphite, Phys. Rev. B **81**, 161403(R) (2010).

[34] B. Pamuk, J. Baima, F. Mauri, and M. Calandra, Magnetic gap opening in rhombohedral-stacked multilayer graphene from first principles, Phys. Rev. B **95**, 075422 (2017).

[35] Y.-Z. Chou, F. Wu, J. D. Sau, and S. Das Sarma, Acoustic-Phonon-Mediated Superconductivity in Rhombohedral Trilayer Graphene, Phys. Rev. Lett. **127**, 187001 (2021).

[36] A. Ghazaryan, T. Holder, M. Serbyn, and E. Berg, Unconventional Superconductivity in Systems with Annular Fermi Surfaces: Application to Rhombohedral Trilayer Graphene, Phys. Rev. Lett. **127**, 247001 (2021).

[37] S. Chatterjee, T. Wang, E. Berg, and M. P. Zaletel, Inter-valley coherent order and isospin fluctuation mediated superconductivity in rhombohedral trilayer graphene, Nat. Commun. **13**, 6013 (2022).

[38] Z. Dong and L. Levitov, Superconductivity in the vicinity of an isospin-polarized state in a cubic Dirac band, arXiv:2109.01133.

[39] W. Qin, C. Huang, T. Wolf, N. Wei, I. Blinov, and A. H. MacDonald, Functional renormalization group study of superconductivity in rhombohedral trilayer graphene, arXiv:2203.09083.

[40] Y.-Z. You and A. Vishwanath, Kohn-Luttinger superconductivity and intervalley coherence in rhombohedral trilayer graphene, Phys. Rev. B **105**, 134524 (2022).

[41] T. Cea, P. A. Pantaleón, V. O. T. Phong, and F. Guinea, Superconductivity from repulsive interactions in rhombohedral trilayer graphene: A Kohn-Luttinger-like mechanism, Phys. Rev. B **105**, 075432 (2022).

[42] A. L. Szabó and B. Roy, Metals, fractional metals, and superconductivity in rhombohedral trilayer graphene, Phys. Rev. B **105**, L081407 (2022).

[43] H. Dai, R. Ma, X. Zhang, and T. Ma, Quantum Monte Carlo study of superconductivity in rhombohedral trilayer graphene under an electric field, arXiv:2204.06222.

[44] Y.-Z. Chou, F. Wu, J. D. Sau, and S. Das Sarma, Acoustic-phonon-mediated superconductivity in Bernal bilayer graphene, Phys. Rev. B **105**, L100503 (2022).

[45] W. Kohn and J. M. Luttinger, New Mechanism for Superconductivity, Phys. Rev. Lett. **15**, 524 (1965).

[46] S. Maiti and A. V. Chubukov, Superconductivity from repulsive interaction, in *AIP Conference Proceedings* (American Institute of Physics, Melville, New York, 2013), Vol. 1550, pp. 3–73.

[47] M. Y. Kagan, V. A. Mitskan, and M. M. Korovushkin, Anomalous superconductivity and superfluidity in repulsive fermion systems, Phys. Usp. **58**, 733 (2015).

[48] S. Raghu, S. A. Kivelson, and D. J. Scalapino, Superconductivity in the repulsive Hubbard model: An asymptotically exact weak-coupling solution, Phys. Rev. B **81**, 224505 (2010).

[49] W. Cho, R. Thomale, S. Raghu, and S. A. Kivelson, Band structure effects on the superconductivity in Hubbard models, Phys. Rev. B **88**, 064505 (2013).

[50] A. V. Chubukov and S. A. Kivelson, Superconductivity in engineered two-dimensional electron gases, Phys. Rev. B **96**, 174514 (2017).

[51] J. González, Kohn-luttinger superconductivity in graphene, Phys. Rev. B **78**, 205431 (2008).

[52] M. L. Kiesel, C. Platt, W. Hanke, D. A. Abanin, and R. Thomale, Competing many-body instabilities and unconventional superconductivity in graphene, Phys. Rev. B **86**, 020507(R) (2012).

[53] R. Nandkishore, L. Levitov, and A. Chubukov, Chiral superconductivity from repulsive interactions in doped graphene, Nat. Phys. **8**, 158 (2012).

[54] N. B. Kopnin, T. T. Heikkilä, and G. E. Volovik, High-temperature surface superconductivity in topological flat-band systems, Phys. Rev. B **83**, 220503(R) (2011).

[55] N. B. Kopnin, M. Ijäs, A. Harju, and T. T. Heikkilä, High-temperature surface superconductivity in rhombohedral graphite, Phys. Rev. B **87**, 140503 (2013).

[56] D.-C. Lu, T. Wang, S. Chatterjee, and Y.-Z. You, Correlated metals and unconventional superconductivity in rhombohedral trilayer graphene: A renormalization group analysis, Phys. Rev. B **106**, 155115 (2022).

[57] K. G. Wirth, J. B. Hauck, A. Rothstein, D. Siebenkotten, L. Klebl, A. Fischer, B. Beschoten, C. Stampfer, L. Waldecker, D. M. Kennes, and T. Taubner, Experimental observation of ABCB stacked tetralayer graphene, ACS Nano **16**, 16617 (2022).

[58] F. Guinea, A. H. Castro Neto, and N. M. R. Peres, Electronic states and Landau levels in graphene stacks, Phys. Rev. B **73**, 245426 (2006).

[59] J. McClure, Electron energy band structure and electronic properties of rhombohedral graphite, Carbon **7**, 425 (1969).

[60] M. S. Dresselhaus and G. Dresselhaus, Intercalation compounds of graphite, Adv. Phys. **51**, 1 (2002).

[61] T. T. Heikkilä and G. E. Volovik, Dimensional crossover in topological matter: Evolution of the multiple Dirac point in the layered system to the flat band on the surface, JETP Lett. **93**, 59 (2011).

[62] T. T. Heikkilä, N. B. Kopnin, and G. E. Volovik, Flat bands in topological media, JETP Lett. **94**, 233 (2011).

[63] U. Zondiner, A. Rozen, D. Rodan-Legrain, Y. Cao, R. Queiroz, T. Taniguchi, K. Watanabe, Y. Oreg, F. von Oppen, A. Stern, E. Berg, P.Jarillo-Herrero, and S. Ilani, Cascade of phase

transitions and Dirac revivals in magic-angle graphene, Nature **582**, 203 (2020).

[64] E. Pangburn, L. Haurie, A. Crépieux, O. A. Awoga, A. M. Black-Schaffer, C. Pépin, and C. Bena, Superconductivity in monolayer and few-layer graphene: I. Review of possible pairing symmetries and basic electronic properties, arXiv:2211.05146.

[65] S. Raghu and S. A. Kivelson, Superconductivity from repulsive interactions in the two-dimensional electron gas, Phys. Rev. B **83**, 094518 (2011).

[66] N. Read and D. Green, Paired states of fermions in two dimensions with breaking of parity and time-reversal symmetries and the fractional quantum Hall effect, Phys. Rev. B **61**, 10267 (2000).

[67] M. Alidoust, M. Willatzen, and A.-P. Jauho, Symmetry of superconducting correlations in displaced bilayers of graphene, Phys. Rev. B **99**, 155413 (2019).

[68] Y.-Z. Chou, F. Wu, J. D. Sau, and S. Das Sarma, Acoustic-phonon-mediated superconductivity in moiréless graphene multilayers, Phys. Rev. B **106**, 024507 (2022).

[69] B. T. Zhou, S. Egan, D. Kush, and M. Franz, Non-Abelian topological superconductivity in maximally twisted double-layer spin-triplet valley-singlet superconductors, arXiv:2206.05599.

[70] J. Jung, M. Polini, and A. H. MacDonald, Persistent current states in bilayer graphene, Phys. Rev. B **91**, 155423 (2015).

[71] A. A. Zibrov, P. Rao, C. Kometter, E. M. Spanton, J. I. A. Li, C. R. Dean, T. Taniguchi, K. Watanabe, M. Serbyn, and A. F. Young, Emergent Dirac Gullies and Gully-Symmetry-Breaking Quantum Hall States in *ABA* Trilayer Graphene, Phys. Rev. Lett. **121**, 167601 (2018).

[72] J. Jung and A. H. MacDonald, Accurate tight-binding models for the π bands of bilayer graphene, Phys. Rev. B **89**, 035405 (2014).

[73] F. Zhang, B. Sahu, H. Min, and A. H. MacDonald, Band structure of ABC-stacked graphene trilayers, Phys. Rev. B **82**, 035409 (2010).

[74] M. Koshino and E. McCann, Trigonal warping and Berry's phase $N\pi$ in ABC-stacked multilayer graphene, Phys. Rev. B **80**, 165409 (2009).

[75] M. Koshino, Interlayer screening effect in graphene multilayers with ABA and ABC stacking, Phys. Rev. B **81**, 125304 (2010).

[76] M. Koshino and E. McCann, Gate-induced interlayer asymmetry in ABA-stacked trilayer graphene, Phys. Rev. B **79**, 125443 (2009).

[77] N. F. Q. Yuan, H. Isobe, and L. Fu, Magic of high-order van Hove singularity, Nat. Commun. **10**, 5769 (2019).

[78] T. Fukui, Y. Hatsugai, and H. Suzuki, Chern numbers in discretized Brillouin zone: Efficient method of computing (spin) Hall conductances, J. Phys. Soc. Jpn. **74**, 1674 (2005).